Pergamon

Int. J. Heat Mass Transfer. Vol. 38, No. 12, pp. 2269–2279, 1995

0017–9310/95 $9.50+0.00

0017–9310(94)00335–1

Onset of Marangoni convection in a layer of fluid modulated by a weak nonplanar oscillatory shear

A. C. OR and R. E. KELLY†

Department of Mechanical, Aerospace and Nuclear Engineering, University of California,
Los Angeles, CA 90024-1597, U.S.A.

(*Received* 8 *November* 1993 *and in final form* 7 *October* 1994)

Abstract—Onset of Marangoni convection in a horizontal layer of fluid possessing a deformable free surface and subjected to a nonplanar oscillation of shear due to motion of the lower plate is studied. Results show that the onset of the Pearson mode occurring at finite wavelengths is delayed by the nonplanar shear, but also that the long-wavelength mode, originally studied by Scriven and Sternling, is destabilized. The modulational effect peaks at a finite frequency and tends to zero in both small and large frequency limits. Physical mechanisms for both stabilization and destabilization are discussed.

1. INTRODUCTION

Thermocapillary instabilities in a layer of liquid giving rise to Marangoni convection are well-known. While Bénard was the first to observe such a phenomenon in a laboratory experiment, which he orginally thought of as being buoyancy-driven, Pearson [1] was the first to offer a systematic theory based on surface-tension effects. For a liquid possessing a negative surface-tension derivative with respect to temperature, Pearson showed that heating the layer from below can yield steady convection if the Marangoni number is above a critical value. Since the effect of gravity cannot in general be ignored, Nield [2] extended the computations by including the buoyancy-driven Rayleigh–Bénard mode. A second important theoretical contribution came from Scriven and Sternling [3], who showed that, by allowing the layer's surface to deform, an instability in the form of long-wavelength disturbances can occur. This mode was later shown by Smith [4] to be stabilizable by gravity. Goussis and Kelly [5] investigated the physical mechanisms for the two convection modes and showed that in some parameter regimes the modes become distinct and well-separated by a stable region.

The effect upon instability of oscillatory motions induced on the layer has not yet been examined. Interest in the effect is actually two-fold: (i) because thermocapillary instabilities can crucially affect materials processing, such as crystal-growth in a space environment [6], the behavior of the instabilities when subject to small-amplitude vibrations is definitely relevant and should be understood; (ii) because convective motions are sometimes undesirable, it is of interest to have a simple means of controlling their onset. Kelly proposed a method of stabilizing a gravitationally unstable layer by a nonplanar oscillatory shear [7]. Kelly and Hu [8] showed that the method tends to stabilize Rayleigh–Bénard convection based on a small Reynolds-number analysis, and in a later paper [9], they demonstrated that significant stabilization can be realized in principle at larger values of Reynolds number. The major purpose of our study is to examine this technique when applied to Marangoni convection. Our approach consists of using a small Reynolds number expansion and then solving the linear stability problem by a Runge–Kutta shooting technique. The buoyancy effect will also be included, although it must be considered to be relatively weak for the deformable case in order to use the Boussinesq model [10].

2. MATHEMATICAL FORMULATION

Consider a horizontal layer with mean depth h of viscous and incompressible fluid heated from below. The Oberbeck–Boussinesq equations describing the system are

$$\mathbf{V}^*_t + \mathbf{V}^* \cdot \nabla \mathbf{V}^* = -\frac{1}{\rho_0} \nabla P^* + g(1-\alpha(T^*-T^*_0))\mathbf{k} + \nu \nabla^2 \mathbf{V}^* \quad (1a)$$

$$T^*_t + \mathbf{V}^* \cdot \nabla T^* = \kappa \nabla^2 T^* \quad (1b)$$

$$\nabla \cdot \mathbf{V}^* = 0. \quad (1c)$$

Let x^* and y^* denote spatial coordinates in the horizontal plane and z^* be the distance normal to the layer, with its positive direction pointing in the same

---

† Author to whom correspondence should be addressed.

NOMENCLATURE

D	derivative with respect to z
g	gravitational acceleration
h	layer depth
k	wavenumber
K	thermal conductivity
$\mathbf{i}, \mathbf{j}, \mathbf{k}$	coordinate unit vectors
N	amplitude of surface deformation
p	pressure
P	pressure associated with basic state
q	heat transfer coefficient at free surface
t	time
T	temperature
$U(z,t)$, $V(z,t)$	x, y components of basic flow velocity
$\mathbf{V}$	vector fluid velocity
w	vertical perturbation velocity
W	amplitude of w
x, y, z	Cartesian coordinates.

Greek symbols

α	coefficient of thermal expansion
β	square-root of the nondimensional oscillation frequency
γ	magnitude of surface tension derivative
δ	phase angle between transverse components of shear
η	surface elevation
Θ	amplitude of perturbation temperature
θ	perturbation temperature, also angle of the wave vector
κ	thermal diffusivity
Λ	modulation parameter
λ	amplitude ratio of Reynolds numbers (Re_y/Re_x)
ν	kinematic viscosity
ρ_0	reference density of fluid
σ	surface tension
Φ	complex mean flow function
ϕ_c, ϕ_s	cosine and sine mean flow functions
∇	gradient operator
$\nabla_\perp^2$	horizontal Laplacian operator
ω	frequency.

Nondimensional parameters

Pr	Prandtl number, ν/κ
Bo	Bond number, $\rho g h^2/\sigma$
Bi	Biot number, qh/K
C	Crispation number, $\rho\nu\kappa/\sigma h$
M	Marangoni number, $\gamma\Delta T^* h/\rho\nu\kappa$
Ra	Rayleigh number, $\alpha g \Delta T^* h^3/\nu\kappa$
Re	Reynolds number, $U_0^* h/\nu$
l	nondimensional layer thickness, $(Bo/2Pr\ C)^{1/3}$.

Superscripts and subscripts

$*$	dimensional quantities
$+$	adjoint or complex conjugate of transpose
0	reference quantity
x, y, z	derivative with respect to x, y, z respectively; also components in x, y, z directions
$(.)'$	derivative with respect to z
$(.)_c$	critical condition.

direction as gravity and measured from the mean free surface level ($z^* = 0$).

The basic state consists of a periodic flow parallel to the plane which has a frequency ω^* and depends on z^* and t^* only. It is generated by a wall oscillation in the x^* and y^* plane at $z^* = \mathrm{h}$. In component form, the basic flow is

$$\mathbf{V}^*(z^*, t^*) = \mathbf{i}U^*(z^*, t^*) + \mathbf{j}V^*(z^*, t^*) \tag{2}$$

governed by the equation

$$2\beta^2 \frac{\partial}{\partial t}\mathbf{V}^* = \frac{\partial^2}{\partial z^2}\mathbf{V}^* \tag{3}$$

where $z = z^*/h$, $t = w^*t^*$, and $\beta^2 = \omega^* h^2/(2\nu)$. The mean flow is then determined by applying a no-slip condition at the wall and a stress-free condition at the free surface so that

$$U^*(1,t) = U_0^* \cos t \quad \frac{\partial}{\partial z}U^*(0,t) = 0 \tag{4a}$$

$$V^*(1,t) = V_0^* \cos(t+\delta) \quad \frac{\partial}{\partial z}V^*(0,t) = 0 \tag{4b}$$

where δ is a phase shift allowed between the two components of wall velocity. An exact solution of the mean flow is available, given by

$$U^*(z,t) = U_0^*\{\phi_c(z)\cos t + \phi_s(z)\sin t\} \tag{5a}$$

$$V^*(z,t) = V_0^*\{\phi_c(z)\cos(t+\delta) + \phi_s(z)\sin(t+\delta)\} \tag{5b}$$

where ϕ_c and ϕ_s are respectively determined as

$$\phi_c(z) = \frac{1}{2}\left\{\frac{\cosh(1+i)\beta z}{\cosh(1+i)\beta} + \frac{\cosh(1-i)\beta z}{\cosh(1-i)\beta}\right\}$$

$$\phi_s(z) = i\frac{1}{2}\left\{\frac{\cosh(1+i)\beta z}{\cosh(1+i)\beta} - \frac{\cosh(1-i)\beta z}{\cosh(1-i)\beta}\right\}. \tag{5c}$$

The scale of the Stokes layer relative to h is determined by β^{-1}. The Oberbeck–Boussinesq system involves the assumption of small viscous dissipation; thus the temperature T^* remains conductive in the absence of convection. The temperature profile even in the presence of a parallel flow is then given by

$$T^*(z^*) = T^*(h) + \Delta T^* T \quad T = z-1$$
$$P^* = \rho g h P \quad P = z \tag{6}$$

where $\Delta T^* = T^*(h) - T_0^*$. Next, we obtain the stability equations by perturbing the flow fields about the basic state. Nondimensional variables will be introduced here. We let

$$\mathbf{V}^*(z,t) = \mathbf{i}\left\{U_0^* U(z,t) + \left(\frac{v}{h}\right)u\right\} + \mathbf{j}\left\{V_0^* V(z,t) + \left(\frac{v}{h}\right)v\right\} + \mathbf{k}\left(\frac{v}{h}\right)w \tag{7}$$

$$T^*(z) = T^*(1) + \Delta T^*(T+\theta) \quad P^* = \rho g h P + \rho\left(\frac{v}{h}\right)^2 p \tag{8}$$

where u, v, w and θ are perturbation variables. After substituting the above expressions into equation (1) and linearizing about the basic state, we can obtain the following equations for w and θ:

$$\left\{2\beta^2\frac{\partial}{\partial t} + Re_x U\frac{\partial}{\partial x} + Re_y V\frac{\partial}{\partial y} - \nabla^2\right\}\nabla^2 w - \left(Re_x U''\frac{\partial}{\partial x} + Re_y V''\frac{\partial}{\partial y}\right)w = -Pr^{-1} Ra \nabla_\perp^2\theta \tag{9}$$

$$Pr\left\{2\beta^2\frac{\partial}{\partial t} + Re_x U\frac{\partial}{\partial x} + Re_y V\frac{\partial}{\partial y}\right\}\theta - \nabla^2\theta = -Pr\, w \tag{10}$$

where the Reynolds number (Re), Prandtl number (Pr) and Rayleigh number (Ra) are defined in the Nomenclature. We consider the lower wall as rigid and isothermal, so that the boundary conditions there are

$$w = w_z = \theta = 0 \quad \text{at}\ z = 1. \tag{11}$$

The boundary conditions at the free surface are determined by five equations, which comprise the normal stress and the two shear stress conditions, the heat flux condition and the kinematic condition. For thermocapillary processes, we consider the surface tension force as varying linearly with temperature at the surface, that is

$$\sigma = \sigma_0 - \gamma(T^*(\eta) - T_0^*) \quad \gamma = -\left(\frac{d\sigma}{dT^*}\right)_0 \tag{12}$$

where γ is typically positive. Upon linearizing about the basic state at $z = 0$, these boundary conditions are, respectively,

$$Re_x U'\eta_x + Re_y V'\eta_y - \frac{Bo\,\eta}{2Pr\,C} + w_z$$
$$-\frac{1}{2}p + \frac{1}{2}\frac{1}{Pr\,C}\nabla_\perp^2\eta = 0 \tag{13}$$

$$Re_x U''\eta + u_z + w_x = Pr^{-1}M(T'\eta_x + \theta_x) \tag{14}$$

$$Re_y V''\eta + v_z + w_y = Pr^{-1}M(T'\eta_y + \theta_y) \tag{15}$$

$$Bi(T'\eta + \theta) = \theta_z \tag{16}$$

$$2\beta^2\eta_t + Re_x U\eta_x + Re_y V\eta_y = w. \tag{17}$$

where C, Bo, M, and Bi are, respectively, the Crispation, Bond, Marangoni and Biot numbers and are defined in the Nomenclature. Both the Crispation number and the Bond number measure the rigidity of the surface due to surface tension, the former with respect to diffusive effects and the latter relative to gravity. The Biot number measures the heat-transfer property of the surface. For $Bi = 0$, the surface is insulating, strictly speaking, but in applying this condition to the stability problem we are thinking of the case of a fixed heat flux. As $Bi \to \infty$, the surface tends to a perfect conductor.

Since the conservation equations consist of w and θ only, u, v and p are eliminated in the stress conditions in favor of w, θ and η; η is related to w through the kinematic condition. In doing the elimination, we combine the x and y components of the momentum equations to give

$$(2\beta^2 w_{zt} + Re_x U w_{zx} + Re_y V w_{zy}) - \nabla^2 w_z = \nabla_\perp^2 p. \tag{18}$$

This expression, together with the continuity equation, is used to recast the normal stress and the tangential stress conditions as, respectively,

$$Re_x(U w_{zx} - 2U'\nabla_\perp^2\eta_x) + Re_y(V w_{zy} - 2V'\nabla_\perp^2\eta_y) + 2\beta^2 w_{zt} - (w_{zzz} + 3\nabla_\perp^2 w_z) + \frac{1}{Pr\,C}(Bo - \nabla_\perp^2)\nabla_\perp^2\eta = 0 \tag{19}$$

and

$$Re_x U''\eta_x + Re_y V''\eta_y + \nabla_\perp^2 w - w_{zz} = Pr^{-1}M\nabla_\perp^2(T'\eta + \theta). \tag{20}$$

Now let

$$(w, \theta, \eta) = (W(z,t), \Theta(z,t), N(t))\,\mathrm{e}^{i(k_x x + k_y y)} + \text{c.c.} \tag{21}$$

where c.c. denotes complex conjugate. After substituting equation (21), the governing equations become

$$\left\{2\beta^2\frac{\partial}{\partial t} + ik_x Re_x U + ik_y Re_y V - \left(\frac{\partial^2}{\partial z^2} - k^2\right)\right\} \times \left(\frac{\partial^2}{\partial z^2} - k^2\right)W - (ik_x Re_x U'' + ik_y Re_y V'')W = Pr^{-1} Ra\, k^2\Theta \tag{22}$$

$$Pr\left\{2\beta^2\frac{\partial}{\partial t}+ik_xRe_xU+ik_yRe_yV\right\}\Theta$$

$$-\left(\frac{\partial^2}{\partial z^2}-k^2\right)\Theta = -Pr\,W \quad (23)$$

to be solved subject to the wall boundary conditions (at $z = 1$)

$$W=\frac{\partial}{\partial z}W=\Theta=0 \quad (24)$$

the free surface stress conditions (at $z = 0$)

$$\left(2\beta^2\frac{\partial^2}{\partial t\,\partial z}-\frac{\partial^3}{\partial z^3}+3k^2\frac{\partial}{\partial z}\right)W-\frac{k^2}{Pr\,C}(Bo+k^2)N$$

$$= -ik_xRe_x\left(U\frac{\partial}{\partial z}W+2k^2U'N\right)$$

$$-ik_yRe_y\left(V\frac{\partial}{\partial z}W+2k^2V'N\right) \quad (25)$$

$$\frac{\partial^2}{\partial z^2}W+k^2W-Pr^{-1}Mk^2(N+\Theta)$$

$$= (ik_xRe_xU''+ik_yRe_yV'')N \quad (26)$$

and the free surface temperature and kinematic conditions

$$\frac{\partial}{\partial z}\Theta-B_i(N+\Theta)=0 \quad (27)$$

$$2\beta^2\frac{\partial}{\partial t}N-W = -(ik_xRe_xU+ik_yRe_yV)N \quad (28)$$

where $k^2 = k_x^2+k_y^2$.

3. THE SMALL-AMPLITUDE EXPANSION

In the following, we present an expansion procedure for the solution of the above system in terms of the Reynolds number, which is assumed to be small. The procedure is very similar to that used by Kelly and Hu [8] for the case of Rayleigh–Bénard convection, and so only a summary of the procedure is presented. We let $Re_x = Re$, $Re_y = \lambda Re$, and expand in terms of Re as follows:

$$W(z,t) = W_0(z)+Re\,W_1(z,t)+Re^2W_2(z,t)+\dots \quad (29a)$$

$$\Theta(z,t) = \Theta_0(z)+Re\,\Theta_1(z,t)+Re^2\Theta_2(z,t)+\dots \quad (29b)$$

$$N(t) = N_0+Re\,N_1(t)+Re^2N_2(t)+\dots \quad (29c)$$

where we have assumed that as $M \to M_c$, a monotonic onset occurs as $Re \to 0$ [1–5]. The critical values of the parameters, Ra_c and M_c, will also be expanded in Re; thus we have

$$M_c = M_0+Re\,M_1+Re^2M_2+\dots \quad (29d)$$

$$Ra_c = Ra_0+Re\,Ra_1+Re^2Ra_2+\dots \quad (29e)$$

The unmodulated neutral curves corresponding to both controls are given in Nield [2]. The modulated neutral curves corresponding to $M = 0$ and a nonslip, nondeformable upper surface are given by Kelly and Hu [8]. For modes corresponding to monotonic growth, the following governing equations hold at $Re = 0$:

$$(D^2-k^2)^2W_0 = -Pr^{-1}k^2Ra_0\Theta_0 \quad (30a)$$

$$(D^2-k^2)\Theta_0 = Pr\,W_0 \quad (30b)$$

where at $z = 1$

$$W_0 = D\,W_0 = \Theta_0 = 0 \quad (31a)$$

and at $z = 0$

$$-D^3W_0+3k^2DW_0-\frac{k^2}{Pr\,C}(Bo+k^2)N_0 = 0 \quad (31b)$$

$$D^2W_0+k^2W_0-Pr^{-1}M_0k^2(N_0+\Theta_0) = 0 \quad (31c)$$

$$D\Theta_0-Bi(N_0+\Theta_0) = 0 \quad (31d)$$

$$W_0 = 0. \quad (31e)$$

From condition (31b), we observe that $N_0 \to 0$ as $Pr\ C \to 0$ if $(Bo+k^2)$ remains finite. If both $(Bo+k^2) \to 0$ and $Pr\ C \to 0$, then N_0 can remain finite. Thus, in general the nondeformable stress free surface condition is realized as $Pr\ C \to 0$, in which we recover the boundary condition used in [1–2]. For $Ra = 0$, simple closed form expressions exist for the dependent variables and the neutral curve [11]. Here, the zeroth-order and the higher order solutions will be obtained by a fourth-order Runge–Kutta shooting method. A critical stability curve is thereby generated in the Ra_0–M_0 plane when all other parameters are held fixed, along which the wavenumber is given by k_c.

For neutrally stable solutions, we can show that both $Ra_1 = 0$ and $M_1 = 0$ by symmetry considerations, and as a result the $O(Re)$ solution is periodic in time with the frequency of the imposed motion. The nonhomogeneous boundary value problem arising at $O(Re)$ was solved numerically. We now proceed to the next order, $O(Re^2)$, at which order a solvability condition for M_2 can be derived from the time-averaged equations. Letting $\overline{W_2}$ and $\overline{\Theta_2}$ be the mean parts of the second-order flow and thermal field, we have the following governing equations

$$(D^2-k^2)^2\overline{W_2}+Pr^{-1}k^2Ra_0\overline{\Theta_2} = -Pr^{-1}k^2Ra_2\Theta_0$$

$$+i\overline{[(k_xU+\lambda k_yV)(D^2-k^2)W_1-(k_xU''+\lambda k_yV'')W_1]} \quad (32a)$$

$$(D^2-k^2)\overline{\Theta_2}-Pr\,\overline{W_2} = i\,Pr\overline{[(k_xU+\lambda k_yV)\Theta_1]}. \quad (32b)$$

The wall conditions at $z = 1$ for the second-order time-mean quantities are

$$\overline{W_2} = D\overline{W_2} = \overline{\Theta_2} = 0. \tag{33a}$$

The free surface conditions at $z = 0$ are

$$-D^3\overline{W_2}+3k^2D\overline{W_2}-\frac{k^2}{Pr\,C}(Bo+k^2)\overline{N_2}$$

$$= \overline{-ik_x\left(U\frac{\partial}{\partial z}W_1+2k^2U'N_1\right)}$$

$$\overline{-i\lambda k_y\left(V\frac{\partial}{\partial z}W_1+2k^2V'N_1\right)} \tag{33b}$$

$$D^2\overline{W_2}+k^2\overline{W_2}-Pr^{-1}M_0k^2(\overline{N_2}+\overline{\Theta_2})$$

$$= \overline{(ik_xU''+i\lambda k_yV'')N_1} \tag{33c}$$

$$D\overline{\Theta_2}-Bi(\overline{N_2}+\overline{\Theta_2}) = 0 \tag{33d}$$

$$\overline{W_2} = \overline{-(ik_xU+i\lambda k_yV)N_1}. \tag{33e}$$

As in the analysis of Kelly and Hu [8], it can be shown from the governing equations that M_2 and Ra_2 are proportional to a factor Λ, defined as

$$\Lambda(\theta,\lambda,\delta) = (\cos\theta+\lambda\cos\delta\sin\theta)^2+\lambda^2\sin^2\theta\sin^2\delta,$$

$$k_x = k\cos\theta, \quad k_y = k\sin\theta. \tag{34}$$

For the case of stabilization ($M_2 > 0$ $Ra_2 > 0$), the preferred value is obtained by minimizing Λ over θ for a given λ and δ. Without loss of generality, it is sufficient to consider the ratios of M_2/Λ and Ra_2/Λ. The minimal values for Λ when stabilization occurs are discussed in ref. [8]. For simplicity, here we set $\Lambda = 1$, and the numerical results should be viewed with this simplification in mind. In general, when both buoyancy and Marangoni effects are present, Ra_2 and M_2 are not individually determined but are related by the solvability condition. Since the onset is monotonic, this condition is real. In the following, we summarize a shooting scheme which is used here to determine the solvability condition. In short, the system of equations (32a,b)–(33a,b) is expressed in the following vector form,

$$\dot{\mathbf{x}} = \mathbf{Ax}+\mathbf{f}_1+Ra_2\mathbf{f}_2 \tag{35}$$

subject to

$$\mathbf{Qx} = 0 \quad \text{at} \quad z = 1 \quad \text{and} \quad \mathbf{Px} = \mathbf{h}_1+M_2\mathbf{h}_2$$

$$\text{at} \quad z = 0.$$

where $\mathbf{x}$ is the state vector; $\mathbf{f}_j$ and $\mathbf{h}_j$, $j = 1$, 2, are known vector functions. The solvability condition takes the form of

$$M_2-bRa_2 = c \tag{36}$$

where b and c are defined as follows:

$$b = \frac{(\tilde{\mathbf{a}}^+\mathbf{Px}_{\mathrm{p2}})}{(\tilde{\mathbf{a}}^+\mathbf{h}_2)} \quad c = \frac{\tilde{\mathbf{a}}^+(\mathbf{Px}_{\mathrm{p1}}-\mathbf{h}_1)}{(\tilde{\mathbf{a}}^+\mathbf{h}_2)}.$$

The vector $\tilde{\mathbf{a}}$ satisfies $(\mathbf{X}_0^+\mathbf{P}^+)\tilde{\mathbf{a}} = 0$; $\mathbf{X}_0$ is a matrix the column vectors of which form half of the fundamental set of the homogeneous system satisfying the wall condition $\mathbf{Qx} = 0$ at $z = 1$; finally $\mathbf{x}_{\mathrm{p}j}$, $j = 1, 2$, satisfy, respectively,

$$\dot{\mathbf{x}} = \mathbf{Ax}+\mathbf{f}_j, \quad j = 1, 2$$

with $\mathbf{x}_{pj} = 0$ at $z = 1$. In the solvability condition (36), b and c can be evaluated numerically through a scheme described in ref. [12].

4. RESULTS

The basic flow in equation (2) depends on the functions $\phi_c(z)$ and $\phi_s(z)$, which in turn depend upon β. The limit $\beta \to 0$ corresponds to a uniform basic flow (i.e. no shear), which has no effect on convection. In

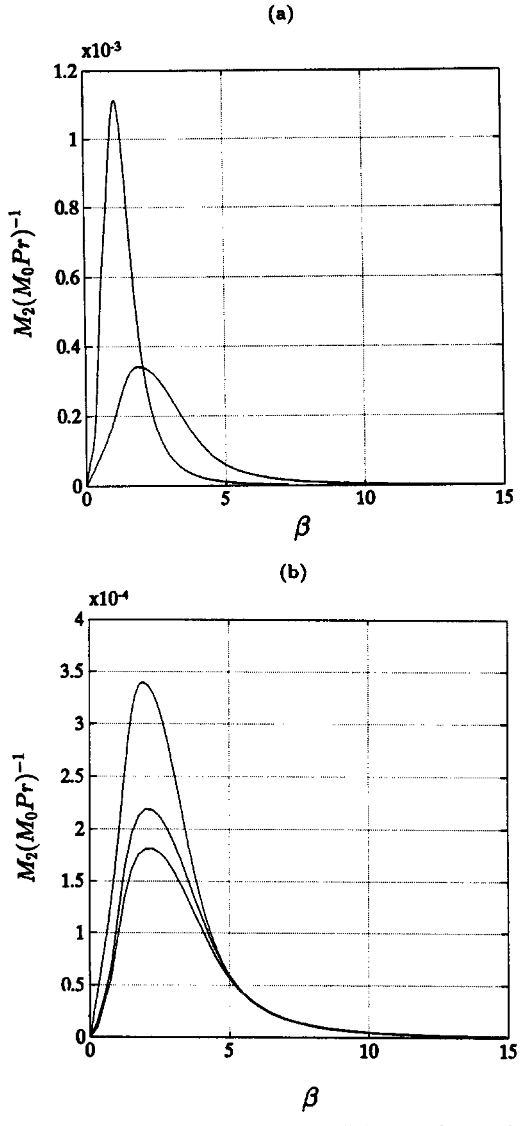

Fig. 1. Modulation curves with negligible surface deformation showing M_2/M_0Pr vs β: (a) $Bi = 0.5$, $Pr = 10$ (higher) and $Pr = 1$ (lower); (b) $Pr = 1$, $Bi = 0.5$ (upper), 10 (middle), and 100 (lower). Steady solutions corresponding to the three curves have $k_c = 2.14$, 2.74, and 2.98 and $M_0 = 98.3$, 413.4 and 3303.8, respectively.

the other limit, as $\beta \to \infty$, both ϕ_c and ϕ_s tend to zero as the Stokes layer becomes vanishingly thin, and so high-frequency oscillations have little effect on convection. Hence, the greatest change in stability due to the oscillation occurs at an intermediate value of β, which typically lies between 1.0 and 2.0.

(i) *Small surface deformations at* Ra = 0

Previous studies [1–5] showed that surface deformations only contribute a higher-order effect to the Pearson mode. To extract the Pearson mode for the present case of deformable boundary conditions, we used a sufficiently small value of the Crispation number (e.g. $C \leqslant 10^{-5}$), so that the surface displacement becomes very small. The problem is then independent of *Bo*. In fact, our results obtained in this way compare extremely well with those corresponding to the non-deformable surface conditions of [1,2]. The small-*Re* analysis consists of determining the $O(Re^2)$ change in M_c from M_0, namely M_2, by evaluating the solvability condition. In Fig. 1, we show M_2, scaled by $M_0 Pr$, as a function of frequency. Figure 1(a) shows the variations with *Pr* at a fixed value of *Bi* when $M_0 = 98.26$ and $k_c = 2.14$ independently of *Pr*. The curves suggest that the stabilizing effect due to the oscillations becomes stronger as *Pr* increases. Next we investigate the variations with *Bi*. For large *Bi*, the surface temperature approaches the ambient temperature T_∞ and so the thermocapillary effect does not exist. In Fig. 1(b), the modulation curves corresponding to three values of *Bi* are plotted. Convection occurs at higher values of M_0 as *Bi* increases. On the other hand, the modulation curves in Fig. 1(b) suggest that a stronger stabilizing effect is associated with a lower *Bi* on the basis of percentage increase of M_c for a given value of *Re*.

(ii) *Significant surface deformation for* Ra = 0

Studies [3–5] show for the zero-shear case that, when the free-surface is allowed to deform, convective instabilities can occur in the long-wavelength limit in addition to the Pearson mode. In ref. [5], a region of stability has been found separating the two unstable modes when *Pr C* is sufficiently small. In presenting the results, there are many different ways to parameterize the family of neutral curves. For example, in ref. [5], the parameterization was done by rescaling the parameters so that the layer thickness *h* appears only in one of them. One advantage of this approach is that the stability gap between the two modes can be identified readily as a function of the layer thickness. Here, we present the results in such a manner that each

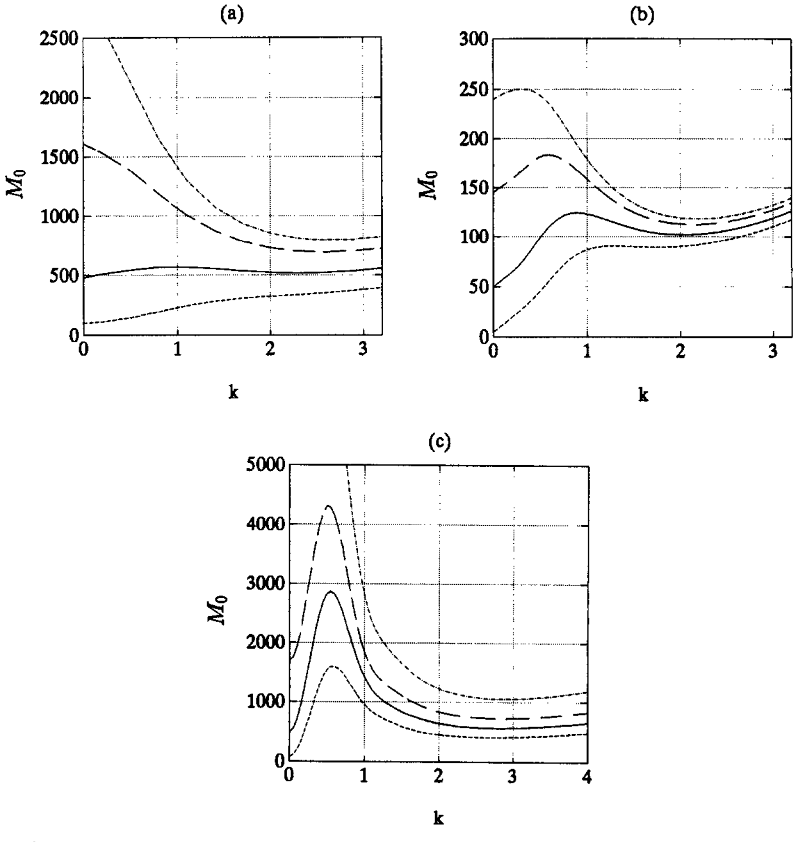

Fig. 2. Steady-state neutral curves at $Pr = 7.0$. Curves in each panel are parameterized in l: 1.0 (short-dashed line), 1.5 (solid line), 2.0 (long-dashed line) and 2.3 for (a, b) but 3.0 for (c) (dashed-dotted line). The values of $Bi\, l^{-1}$ and $2Pr\, C\, l$ for the curves on different panels are: (a) 10, 0.5; (b) 0.5, 0.1; and (c) 10, 0.01.

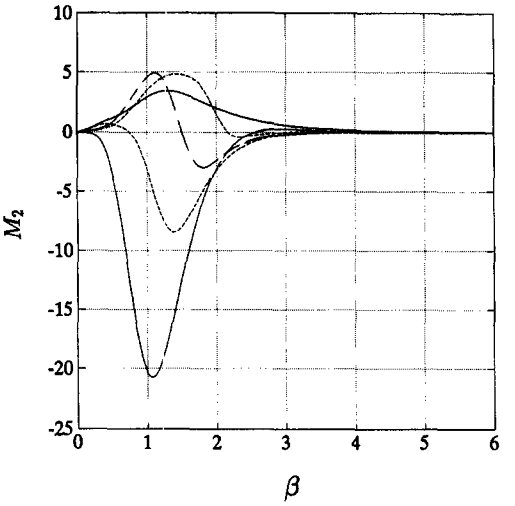

Fig. 3. Characteristic curves for the long-wavelength mode showing M_2 vs for various k: from bottom 0.1 (solid line), 0.5 (short-dashed line), 0.6 (long-dashed line), 0.75 (short-dashed line) and 3.0 (solid line). Other parameters are $Pr = 7.0$, $Bi = 15$, $Bo = 0.0225$ and $C = 4.76 \times 10^{-4}$.

diagram corresponds to a fluid of the same material properties. The family of neutral curves in each diagram then corresponds to different layer thicknesses. The quantity used to parameterize the curves is defined as $l = (Bo/2Pr\ C)^{1/3}$, which is proportional to h but not σ (note that $l^3 = \chi$, the Galileo number, in ref. [5]). Figure 2 consists of three diagrams. Each diagram contains four neutral curves with different l. Since Bi is proportional to h but C is inversely proportional to h, the values of $Bi\ l^{-1}$ and $2Pr\ C\ l$, rather than Bi and C, are given for each diagram. Results in panels (a) and (c) correspond to a better-conducting free surface than in panel (b). Panels (a) and (b) correspond to a larger Crispation number, thus a weaker surface tension than in panel (c). The results of Fig. 2 suggest that the long-wavelength mode is more preferred for a thin layer, unless surface tension is very strong. For a free surface that is a good conductor as well as possessing strong surface tension, the two modes are well-separated by a stable region. At some layer thickness, the two modes can have the same critical Marangoni number, implying that both modes can coexist at the onset. In some other situations, the stable barrier disappears in such a way that $M_0(k)$ almost has the same value for the whole k band.

Having summarized the steady solutions for $Re = 0$, we now consider effects associated with the oscillation. We assume that the modulated onset occurs at the same critical wavenumber as the unmodulated steady onset and consider how the oscillation affects the stability of the two distinct modes. The response for five different wavenumbers is shown by the curves in Fig. 3. A typical value of M_2 for the Pearson mode with $k = 3.0$ is shown by the upper solid curve of Fig. 3. Similarity with the curves in Fig. 1 is evident. Thus, even for significant surface deformations, the qualitative features of the Pearson mode remain unchanged. The effect of the oscillating shear gets stronger as $k \to 0$, with the lower solid curve in Fig. 3 for $k = 0.1$ showing destabilization ($M_2 < 0$) over the range of β for which M_2 is significant. (The values associated with $k = 0$ can be determined by the interpolation method.) The two solid curves represent the two end-values of wavenumbers. Destabilization occurs for the long-wavelengths and stabilization occurs for the short-wavelengths, but the destabilizing effect appears more pronounced. In the intermediate wavenumber regime (e.g. at $k = 0.6$), the curve has both a crest and a trough, and so the trend depends on β. Discussion of the mechanism of the shear which causes stabilization for one mode but destabilization for the other will be postponed to a later section. For the moment, our focus will be on the destabilization of the long-wavelength mode, and its characteristic curves for representative parameters. Figure 4(a) shows, for $Bi = 0.5$–100, the curves of M_2/M_0 almost collapse onto one curve at a small wavenumber. This property suggests that M_2 is roughly proportional to M_0 but that otherwise M_2 is not sensitive to Bi. Comparison of Fig. 4(a) with Fig. 1(b) suggests a stronger explicit dependence of the Pearson mode on Bi. Next, we consider the variation of M_2 with Pr. Figure 4(b) shows three curves varying over two decades of Pr, from 0.07 to 7.0. Again, the curves almost merge into one single curve when M_2/Pr is plotted.

(iii) *The general case for* Ra $\neq 0$

When both buoyancy and thermocapillary forces are present, Nield [2] found that at $Re = 0$ the two effects reinforce rather than oppose one another. Here, we consider a layer with a deformable free surface. But before we present the results, several aspects of the general problem are noted.

First, in order that the Boussinesq approximation be valid, we require $\alpha\Delta T^*$ to be small. Thus, for a layer thickness that corresponds to the long-wavelength mode regime, Ra is typically of $O(10^1)$ or less for neutral stability, and so its effect should be modest in the Boussinesq regime. In some numerical results for the case of a deformable surface, $M_0(k)$ was found to become negative as $k \to 0$ when Ra_0 is sufficiently large, indicating that an instability appears to occur in the long-wavelength limit for pure Rayleigh–Bénard convection. It has been noted elsewhere that this instability cannot exist for values of $\alpha\Delta T^*$ in the Boussinesq regime. In fact, the surface deformation has to be zero for Rayleigh–Bénard convection in the Boussinesq limit (see ref. [10] for example, pp. 40–42).

Second, as pointed out in ref. [13], both M and Ra are proportional to the external heating, which appears to be often the only parameter that can be conveniently varied in an experiment. In fact, both control parameters are related by

$$M = \Gamma\,Ra \quad \Gamma = \frac{\gamma}{\rho_0 \alpha g h^2}. \tag{37}$$

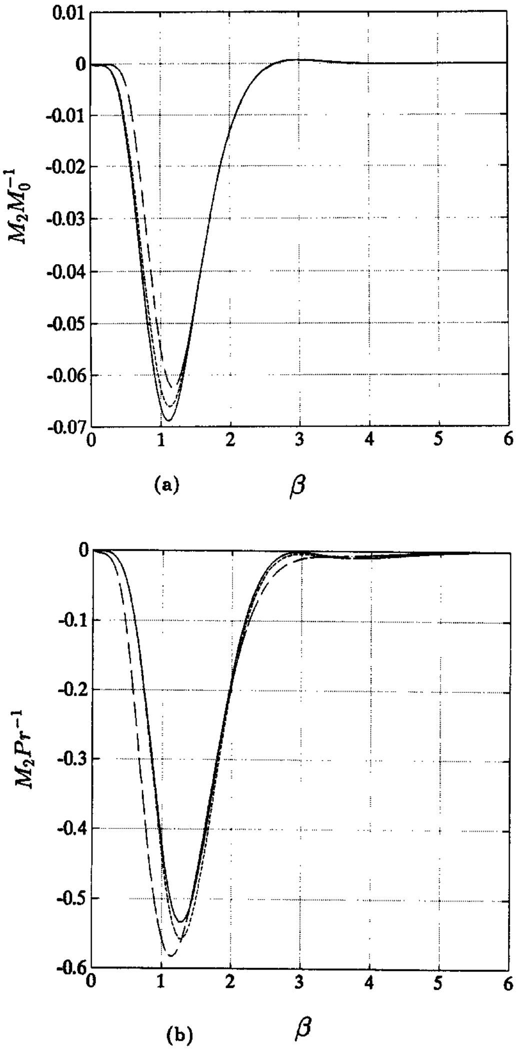

Fig. 4. (a) M_2/M_0 vs β at $k = 0.5$ for different Bi: 0.5 (long-dashed line), 10 (short-dashed line) and 100 (solid line). Other parameters are $Pr = 7.0$, $Bo = 0.5$ and $C = 0.036$. (b) M_2/Pr vs β at k = 1.0 for various Pr: 0.07 (solid), 0.7 (short-dashed line) and 7.0 (long-dashed line). Other parameters are $Bi = 10$, $Bo = 0.5$ and $C = 0.036$.

Therefore, equation (37) typically imposes an additional constraint on the general solvability condition (36) for a given experiment, where Γ is held constant. Solving equation (37) and (36) simultaneously gives

$$M_2 = \frac{c\Gamma}{\Gamma - b} \quad R_2 = \frac{c}{\Gamma - b}. \tag{38}$$

So far, in all the results b is negative and so the denominator does not vanish. Alternatively, the Γ in these expressions can be substituted for by the ratio M_0/Ra_0. The two limits of pure thermocapillary convection and Rayleigh–Bénard convection now correspond respectively to the limiting cases of $|\Gamma| \gg |b|$ and $|\Gamma| \ll |b|$.

Two cases are distinguished in the following results. (i) When $M > 0$ and $Ra > 0$, the typical configuration is one of bottom-heating with the surface tension having $\gamma > 0$ [13]. In this case the thermocapillary and gravitational effects tend to reinforce each other. (ii) When $Ra < 0$, $\Delta T^* < 0$ and therefore the layer is heated from above. For $M > 0$, the liquid is required to have $\gamma < 0$, which is more unusual than case (i). The two cases for $M < 0$ will not be considered here but they have been studied with $Re = 0$ in the literature (for example, see refs. [13] and [14]). In the following, we present some results for cases (i) and (ii) in which the influence of the gravitational effect on thermocapillary convection is emphasized.

In Fig. 5, we take a neutral curve with $Ra = 0$ (solid line) and compare it with one that occurs at $\Gamma = 10$ (short-dashed line) and one that occurs at $\Gamma = -10$ (long-dashed line). In Fig. 5(a), $C = 0.0238$ and in Fig. 5(b), C is 50 times smaller. In Fig. 5(a), we observe that the gravitational effect is small on the neutral curve in the Pearson mode regime, but changes the curve substantially in the long-wavelength regime. As anticipated, gravity is destabilizing for $Ra > 0$ but stabilizing for $Ra < 0$. As the upper surface becomes more rigid, the gravitational effect does not appear to exert a significant influence on the neutral curve in either modal regime [see Fig. 5(b)]. The perturbation effect of the nonplanar oscillatory shear on the steady solution of Fig. 5(a) is then examined. The result is shown in Fig. 6. The stabilizing effect for the larger wavenumbers is slight for Ra of this magnitude. But the destabilizing effect for the smaller wavenumbers depends quite sensitively on gravity. Contrary to the results of Fig. 5(a), now the case for $\Gamma < 0$ is more destabilized than the case for $\Gamma > 0$.

(iv) *Physical mechanisms*

The physical mechanisms associated with the two distinct modes of instability have been discussed by Goussis and Kelly [5]. Here, we are actually more interested in the mechanisms of instability when the unsteady shear flow also plays a role. As the small-Re results indicate, Marangoni convection can be stabilized or destabilized, depending on the preferred wavelength of the steady mode at onset.

We seek to gain insight by examination of energy transfer to the disturbance. In ref. [8], it was demonstrated that a nonplanar shear eliminates the freedom for roll-reorientation which renders the shear ineffective for unidirectional flow as far as changing Ra_c is concerned. However, the stabilizing effect of shear for that case is basically the same as the effect of shear upon transverse disturbances in the 2D case. Therefore, it suffices for us to consider the disturbance energy on the basis of the simpler 2D case. The important sources for energy transfer are given in the surface tangential-stress conditions, equations (14), (15). In the 2D case, take (14), multiply the expression by u and average it over time and the horizontal coordinate ($\langle\cdot\rangle$ denotes such averaging) to obtain

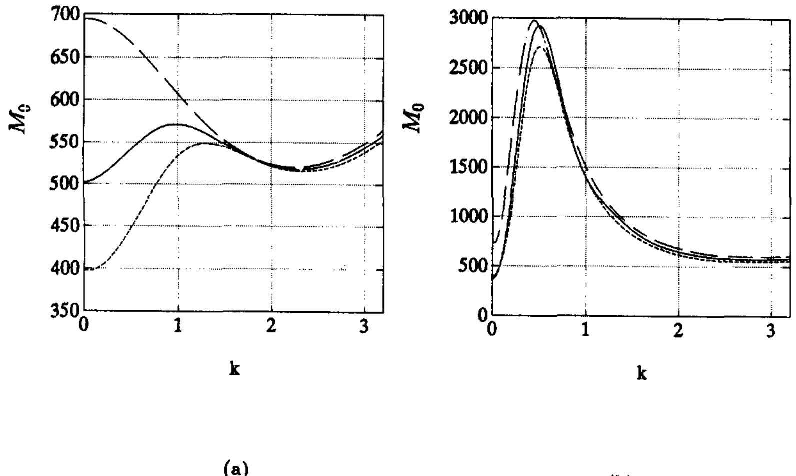

(a) (b)

Fig. 5. Neutral curves showing the effect of finite Ra: parameters in (a) and (b) correspond, respectively, to those of the solid lines in Fig. 2(a) and (c). Here, $Ra = 0$ (solid line), $\Gamma = 10$ (short-dashed line) and $\Gamma = -10$ (long-dashed line).

$$\langle -u(u_z+w_x)\rangle = Re\langle(\phi_c''\cos t+\phi_s''\sin t)u\eta\rangle - Pr^{-1}M\langle u(T'\eta_x+\theta_x)\rangle. \quad (39)$$

Actually, there exists another energy source term corresponding to the Reynolds stress, which is a bulk term and involves integration over the fluid depth. This Reynolds-stress term, like in the case of ref. [8], is at least $O(10^{-4})$ smaller than the others and is therefore neglected. The term on the left hand-side of equation (39), say E_s, represents the work done by the surface shear stress on the fluid. This energy generating term has been found to be balanced almost completely by the viscous dissipation. It is composed of the two terms on the right of equation (39). The first term on the right, say E_b, represents work done by the basic flow shear owing to surface deformation. This term is expected to have little effect on the Pearson mode but can influence the long-wavelength mode. The second term, say E_m, represents the energy release owing to the thermocapillary effect. In an expanded form, to $O(Re^2)$, E_s is given by

$$E_s = E_{s0}+E_{s2}Re^2+\ldots \quad (40)$$

and likewise for E_m. In contrast, E_b is second-order in Re. Thus, these energy terms satisfied

$$E_{s0} = E_{m0} \quad E_{s2} = E_b+E_{m2}. \quad (41)$$

The energy production terms are now illustrated by several sweep-plots vs wavenumber in Figs. 7–8. In Fig. 7, the upper-left panel shows a log–log plot of E_{s0}. This rate of energy production increases as k decreases. The upper-right panel shows the numerical accuracy, in which the magnitude of difference between E_{s0} and E_{m0} is shown. The corresponding energy production in $O(Re^2)$ is shown in the lower-left panel. It is found that E_{s2} increases even more rapidly than E_{s0}. The shape of E_{s2} marks a certain transition in characteristics near $k \approx 0.5$. Again, the lower-right panel shows the numerical accuracy, in which it is shown that the difference between E_{s2} and E_b+E_{m2} is negligibly small. To understand the relative importance between the various components of energy production near the transition and the reason for M_2 switching sign as k decreases, we compare the various energy production terms in Fig. 8. The circles mark the curve of E_{s2}, which is equal to the sum of all other terms. The solid curve represents E_b, which is almost zero for larger k, but increases sharply for k decreasing from about 0.65. The Marangoni term, E_{m2}, consists of two parts: $E_{m2}^{(1)}$ represents the second-order Marangoni shear-stress term, whereas $E_{m2}^{(2)}$ is equal to the product of M_2 and E_{s0}/M_0, namely,

$$E_{m2}^{(2)} = M_2Pr^{-1}\langle u_0(T'\eta_0+\theta_0)_x\rangle. \quad (42)$$

In Fig. 8, the short-dashed curve represents $E_{m2}^{(1)}$,

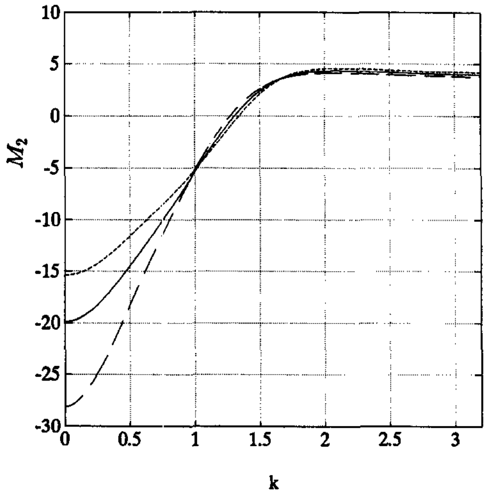

Fig. 6. Showing the M_2 of the neutral curves in Fig. 2(a) at $\beta = 1.2$.

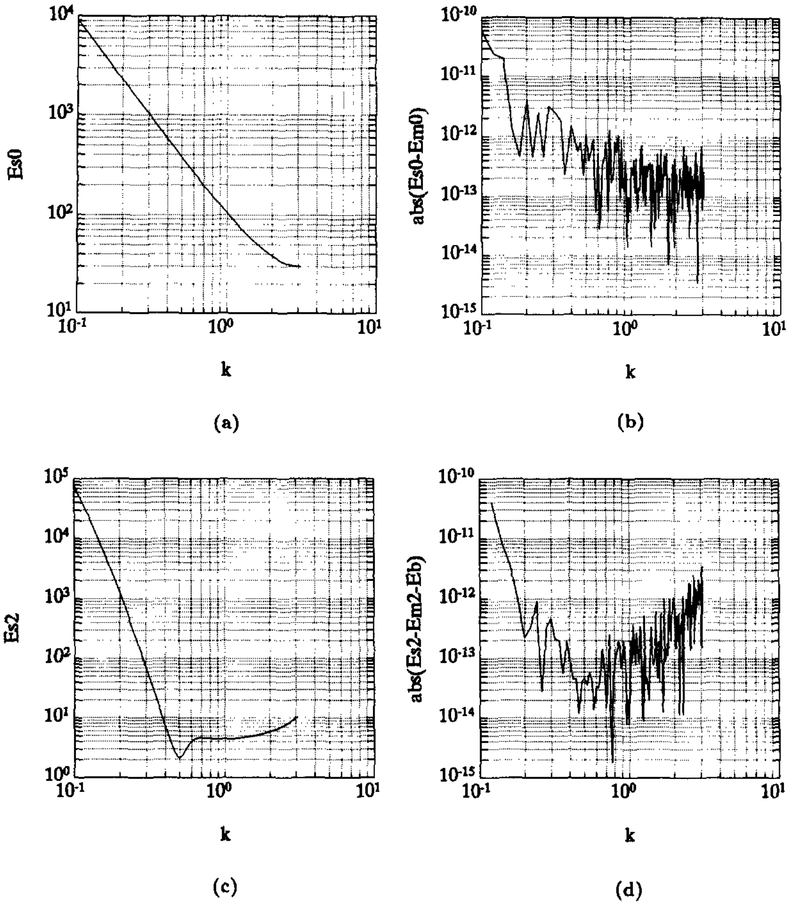

Fig. 7. Log–log plots of energy source terms as functions of wavenumber: (a) E_{s0}; (b) magnitude of $E_{s0}-E_{m0}$; (c) E_{s2}; and (d) magnitude of $E_{s2}-E_{m2}-E_{b}$. The parameters are: $Pr = 7$, $Bi = 15$, $C = 4.76\times10^{-4}$, $Bo = 0.0225$. Panels (b) and (d) are intended for showing the numerical accuracy.

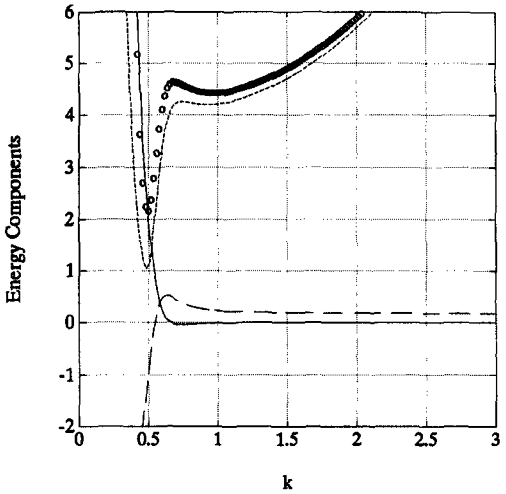

Fig. 8. A comparison of the second-order energy source terms as functions of wavenumber: E_{s2} (circles); E_{b} (solid line); $E^{(1)}_{m1}$ (short-dashed line) and $E^{(2)}_{m1}$ (long-dashed line). The parameters are the same as in Fig. 7.

whereas the long-dashed curve represents $E^{(2)}_{m2}$. Since E_{s0}/M_0 is positive, the sign of M_2 is determined by the sign of $E^{(2)}_{m2}$. Thus, for larger k, $E^{(1)}_{m2}$ falls short of overcoming the dissipation, and therefore the Marangoni number must be increased (corresponding to $M_2 > 0$) to produce a stronger shear for sufficient energy production. At lower k, even though $E^{(1)}_{m2}$ maintains the same pace as the dissipation, a new source of energy, namely, E_{b} arises. In the presence of this additional surface shear generated by the basic flow, the thermocapillary shear responsible for the instability is weaker. Thus, M_2 is negative.

5. CONCLUSIONS

The major findings in our present results are that the Pearson mode, similar to the Rayleigh–Bénard mode, is stabilized by a nonplanar shear oscillation while the long-wavelength mode is destabilized. The stabilization is due to an increase in viscous dissipation associated with non-zero Reynolds number. The Reynolds stress effect is small. The destabilization of the long-wavelength mode, on the other hand, is due to the increase of perturbation shear stress at the surface which in the presence of surface deformation provides an additional source of energy. A time-periodic shear flow with a free surface can produce a long-wavelength mode of instability even for an isothermal situation [15]. In Yih's case [15], instability occurs at a finite value of *Re*, but it appears that the present long-wavelength destabilization and that for Yih's problem may involve the same mechanism. Since in the isothermal case no thermocapillary shear is available, long-wavelength instability can only occur at finite *Re*, when the energy release is sufficiently strong as to overcome dissipation.

The small-*Re* results presented here give us a guide for a finite-*Re* study, which is currently underway. Only by means of such a study can we determine whether the stabilization or destabilization can be significant.

Acknowledgement—This research was supported by the NASA Microgravity Fluid Physics Program through grant NAG3-1456.

REFERENCES

1. J. R. A. Pearson, On convection cells induced by surface tension, *J. Fluid Mech.* **4,** 489–500 (1958).
2. D. A. Nield, Surface tension and buoyancy effects in cellular convection, *J. Fluid Mech.* **19,** 341–352 (1964).
3. L. E. Scriven and C. V. Sternling, On cellular convection driven surface tension gradients: effects of mean surface tension and surface viscosity, *J. Fluid Mech.* **19,** 321–340 (1964).
4. K. A. Smith, On convective instability induced by surface tension, *J. Fluid Mech.* **24,** 401–414 (1966).
5. D. A. Goussis and R. E. Kelly, On the thermocapillary instabilities in a liquid layer heated from below, *Int. J. Heat Mass Transfer* **33** (10), 2237–2245 (1990).
6. S. Ostrach, Fluid mechanics in crystal growth—the 1982 Freeman Scholar Lecture, *J. Fluids Engng* **105,** 5–20 (1983).
7. R. E. Kelly, Stabilization of Rayleigh-Bénard convection by means of a slow nonplanar oscillatory flow, *Phys. Fluids A* **4** (4), 647–648 (1992).
8. R. E. Kelly and H. C. Hu, The onset of Rayleigh–Bénard convection in non-planar oscillatory flows, *J. Fluid Mech.* **249,** 373–390 (1993).
9. R. E. Kelly and H. C. Hu, The effect of finite amplitude nonplanar flow oscillations upon the onset of Rayleigh–Bénard convection, *Heat Transfer* 1994, *Proc.* 10*th Int. Heat Transfer Conf.* **7,** pp. 79–83 (1994).
10. P. G. Drazin and W. H. Reid, Hydrodynamic stability. In *Cambridge Monographs on Mechanics and Applied Mathematics*. Cambridge University Press, Cambridge (1982).
11. S. Screenivasan and S. P. Lin, Surface tension driven instability of a liquid film down a heated incline, *Int. J. Heat Mass Transfer* **21,** 1517–1526 (1978).
12. A. C. Or, A shooting scheme for boundary-value problems, *J. Comput. Phys.* **114**(2), 280–283 (1994).
13. C. Pérez-Garcia and G. Carneiro, Linear stability analysis of Bénard–Marangoni convection in fluids with a deformable free surface, *Phys. Fluids A* **3** (2), 292–298 (1991).
14. M. Takashima, Surface tension driven instability in a horizontal liquid layer with a deformable free surface. II. Overstability, *J. Phys. Soc. Jap.* **50** (8), 2751–2756 (1981).
15. C. S. Yih, Instability of unsteady flows or configurations, Part 1. Instability of a horizontal liquid layer on an oscillating plane, *J. Fluid Mech.* **31,** 737–751 (1968).